Drag Reduction by Manipulation of Afterbody Vortices

D. S. Bulathsinghala[1], Z. Wang[2] and I. Gursul[3]
Department of Mechanical Engineering
University of Bath, Bath, BA2 7AY, UK

Drag force, surface pressure and particle image velocimetry measurements have been carried out in wind tunnel experiments in order to study the effect of mini-spoilers on the drag of an axisymmetric cylinder with a slanted base that has an upsweep angle of $\Phi = 28°$. Two different spoiler heights ($h/D = 2.5\%$ and 5%) were examined at various chordwise locations along the slanted surface. Placing the spoiler closer to the beginning of the slanted section caused an increased drag due to the separation induced by the spoiler itself, although a more diffused afterbody vortex was produced due to the turbulence ingestion. Drag reduction was observed when placing the spoiler closer to the trailing-edge, with the optimum location $x'_s/c = 87.5\%$, resulting in approximately 5% drag reduction for both spoiler heights. This reduction is due to the displacement of the afterbody vortex away from the surface as the mini-spoiler acts similarly to a Gurney flap. The same effect can also be produced by introducing a smaller co-rotating vortex to manipulate the afterbody vortex trajectory.

[1]Postgraduate Research Student, Department of Mechanical Engineering.
[2] Lecturer, Department of Mechanical Engineering.
[3] Professor, Department of Mechanical Engineering.

Nomenclature

ΔC_D	=	change in drag coefficient with flow control
C_{D0}	=	baseline drag coefficient
C_p	=	pressure coefficient
c	=	upsweep chord length
c_{VG}	=	vortex generator chord length
D	=	model fuselage diameter
$\overline{H}$	=	vortex centroid distance from surface
$\overline{H}_{ref}$	=	vortex centroid distance from surface for the baseline case
h	=	spoiler height
h_{VG}	=	vortex generator height
L	=	streamwise length of swept section
Re_D	=	Reynolds number based on diameter
U_∞	=	freestream velocity
u	=	streamwise velocity
v	=	vertical velocity
x	=	streamwise coordinate
x'	=	coordinate along upsweep surface
x'_s	=	spoiler location on upsweep surface
y	=	vertical coordinate
$\overline{y}$	=	vortex centroid location
z	=	spanwise coordinate
z'	=	spanwise coordinate on the upsweep surface
β	=	vortex generator incidence angle
Γ	=	circulation
Λ	=	vortex generator sweep angle
σ	=	standard deviation of velocity magnitude
Φ	=	upsweep angle
ω	=	vorticity

I. Introduction

Fuselage afterbody vortices are more pronounced on cargo aircraft equipped with an aft loading bay due to their larger upsweep angles and result in an additional drag penalty [1]. This problem has received more attention in recent years due to the increased number of long range transport aircraft missions [2]. In addition to the increased drag, the presence of these vortices result in an upwash towards the centerline of the afterbody, which may interfere with airdrop missions [3]. Due to these reasons, it is desirable to find a solution for this afterbody vortex problem by means of flow control.

The flow physics of afterbody vortex flows were first studied experimentally using slanted base cylinder models [4-7]. These models enabled a benchmark afterbody vortex flow to be established between different experimental facilities while not being confined to a single aircraft geometry. The results showed that the flowfield and drag coefficient were highly dependent upon the upsweep angle (Φ is defined in Figure 1a) of the afterbody [4]. Two counter-rotating vortices were present at low upsweep angles (below a critical value between Φ = 45° and 50°) and a separated wake at higher upsweep angles [8]. A recent experimental campaign initiated at the University of Bath revisited the flow physics of afterbody vortex flows on cylinders with slanted bases using Particle Image Velocimetry (PIV) measurements [9]. Tests were performed within two different experimental facilities such that the effects of Reynolds number could be investigated. The effects of angle of attack and yaw on the baseline flowfield were also examined [10], along with the effect of varying the upsweep angle within a range more relevant to military transport aircraft. It was found that the drag coefficient was directly proportional to the vortex strength at the trailing-edge [9].

There have been many attempts at applying flow control with the aim of drag reduction to afterbody vortex flows. During the development of the Short Belfast aircraft, strakes were placed close to the afterbody trailing-edge, resulting in a drag reduction of 7% as identified from wind tunnel tests [11]. These strakes were thought to disrupt the inflow of air into the afterbody region. Vortex generators are also a common passive flow control approach documented within literature, where a favorable interaction between the generated vortex and the afterbody vortex is sought in order to realize a drag reduction. Calarese *et al.* [12] tested a range of passive vortex generators on a scale model of the Lockheed Martin C-130 aircraft, which has an upsweep angle of 28°, and reported drag reduction for specific configurations. Wortmann [13] tested the application of vortex

generators on scale models of Boeing 747 and Lockheed Martin C5 aircraft afterbodies, reporting drag reductions of 3% and 6% respectively. Smith *et al.* [14] carried out their study on the C-130 aircraft, investigating the potential of retrofittable microvanes to reduce afterbody drag. A similar investigation on the potential of finlets and microvanes was computationally carried out by Telli *et al*. [15], suggesting total aircraft drag reductions of 4% for the best microvane configuration. A multi-national effort involving computational simulations and wind tunnel testing suggested a total drag reduction of 1.8% on the C-17 aircraft [16]. There have been limited studies applying active flow control to the afterbody vortex problem. Jackson *et al.* [17] applied different configurations of blowing jets and slots on a $\Phi = 28°$ slanted base cylinder model at a Reynolds number of 20,000 (based on model diameter) in a water tunnel. The best results were obtained with a jet flap parallel to the freestream, giving a 9% drag reduction and 3% overall energy saving.

The current study is an experimental investigation into the use of spoilers as a passive flow control technique in order to reduce afterbody vortex drag on a slanted base cylinder model with an upsweep angle $\Phi = 28°$. The idea of using a spoiler was presented in a review paper by Bearman [8], showing the destruction of the vortex footprint for an upsweep angle of $\Phi = 50°$ on a slanted base cylinder. This large upsweep angle of $\Phi = 50°$ was near the critical upsweep angle between the two different types of wakes as discussed earlier. Similar spoiler or flap applications have been reported on Ahmed bodies, which is a bluff body model with a truncated aft end related to automotive applications that generates a counter-rotating vortex flow structure [18] at slant angles below about 30°. The flow features within the vortex flow regime are broadly similar to the afterbody vortex considered in the current study. Beaudoin and Aider [19] considered an Ahmed body with a 30° slant angle, and studied the effect of a spoiler on the junction of the roof and rear slant, reporting 15% drag reduction for the best deflection angle. Fourrie *et al.* [20] tested a similar spoiler at the same location, and reported a drag reduction of 9% for a base slant angle of 25°. For both studies, the optimum deflector angle was such that the spoiler/flap was almost parallel to the freestream. The spoilers utilized in the current study are perpendicular to the upsweep surface and are of full span at each location. Results are presented in terms of force measurements, pressure measurements and Particle Image Velocimetry (PIV) measurements.

II. Experimental Techniques

The experiments were carried out within the closed return wind tunnel at the Department of Mechanical Engineering, University of Bath. The tunnel has an octagonal cross section with overall dimensions 2.13 m x 1.52 m x 2.70 m. The freestream velocity in the working section was monitored using a pitot static probe mounted within the tunnel connected to a digital manometer. The experiments were carried out at zero incidence at U_∞ = 15 ms^{-1}, which results in a Reynolds number based on the diameter Re_D = 200,000.

A. Wind Tunnel Model

The slanted base cylindrical model utilized for the experiment had an afterbody upsweep angle of Φ = 28°, similar to that of a Lockheed Martin C-130 aircraft. The cylindrical fuselage had a diameter D = 200 mm, which was fabricated from a PVC pipe. It was machined to obtain the required upsweep angle and the base was covered using a 3 mm thick PVC sheet in order to create the elliptical base of the upsweep. A nose-cone was 3D printed using solid laser sintering which consisted of an ellipsoid of 2:1 major to minor axis ratio. The boundary layer was not tripped in the present experiments. We have not observed significant effect of Reynolds number in our experiments in a water tunnel at Re =20,000 [9], which is one order of magnitude smaller than that in the wind tunnel experiments. Britcher and Alcorn [7] compared drag measurements between free transition and fixed transition experiments on a slanted base cylinder, and the effect on the drag was negligible. In addition, Xia and Bearman [6] showed that increasing freestream turbulence did not have a major effect on the vortex flow. All these suggest that, in the case of fixed separation line, the effect of Reynolds number is negligible. This may not be the case for real aircraft as the separation line is not fixed. We estimate the ratio of the boundary layer thickness to the diameter to be around 2% in our experiments.

The model parameters and coordinate axes can be identified in Fig. 1a. A custom made streamlined support structure enabled attaching the model onto a force balance, and allowed pressure taps to be fed through. The combined blockage effect of the model and the support system was 2% of the working section area.

The upsweep section of the model was equipped with 134 surface pressure taps, each of 1.6 mm diameter, in order to map the surface pressure distribution on the upsweep. The taps were distributed along the starboard side of the upsweep with varying spanwise density according to

where the time-averaged vortex was located based on the initial baseline PIV tests. The locations of the surface pressure taps are shown in Fig. 1b.

A schematic of the spoilers tested in the current study is presented in Fig. 2. It was hypothesized that these spoilers would either disrupt the vortex formation directly or act as flow deflectors which alter the overall flowfield. The spoilers were placed perpendicular to the surface and were of full span locally at each chordwise location. Two spoiler heights with h/D = 2.5% and 5% were tested. The spoilers were tested at 20 chordwise locations along the upsweep, from x'_s/c = 2.5% up to x'_s/c = 97.5% with a spacing of $\Delta x'_s/c$ = 5% in-between locations. The spoilers were 3D printed using ABS material and placed onto the model surface using double sided tape.

B. Force Measurements

A single component binocular type strain gauge force balance was utilized to measure the total drag force on the model. This type of design consists of two stress concentration throats onto which the strain gauges are mounted, enabling the measurement of the drag force upon calibration. Drag data was acquired at a sampling frequency of 1 kHz for 10 s with a minimum of 6 repeats at each flow control configuration. Selected cases were repeated on varying days in order to assess the uncertainty in measurement and to check its repeatability. The maximum uncertainty in the measurement of ΔC_D was 2% using the methods outlined by Moffat [21].

C. Pressure Measurements

The time-averaged pressure measurements were performed using a 48 port Scanivalve® multiplexer, connected to a Sensortechnics HCX series differential pressure transducer with an operating range between -10 mbar to +10 mbar. Each mean pressure measurement consisted of data acquired at 1 kHz, with three consecutive repeats per tap.

D. Particle Image Velocimetry (PIV)

The 2D PIV system utilized for the experiments was a TSI® system which consists of a TSI® 610036 synchroniser connected to a 200 mJ Nd:YAG laser. A six jet TSI® 9307 oil droplet generator was used to seed the wind tunnel, where the resulting mean seeding particle diameter was about 1 µm.

The PIV measurements in the crossflow planes were performed on the model at five different stations along the afterbody at x/L = 0.2, 0.4, 0.6, 0.8 and 1.0, which are shown in Fig. 1a. Image

capturing was achieved using a 105 mm f/2.8D Nikon lens attached to a 8MP Powerview Plus CCD camera capturing 500 instantaneous image pairs at a capture frequency of about 3.75 Hz. Image processing was achieved using the TSI® Insight 3G software, the Hart cross-correlation algorithm was applied with a 48x48 interrogation area with 50% overlap. Spatial resolution varied between 0.9 mm and 1.4 mm between measurements, less than 1% of the model fuselage diameter. Assuming model alignment and flow symmetry, the starboard side vortex was captured in the crossflow PIV results. The PIV camera was positioned downstream of the model within a transparent perspex box with the laser mounted on a traverse system perpendicular to the freestream (Fig. 3a).

In addition to the PIV measurements in crossflow planes, measurements were made on the streamwise $z = 0$ plane (model symmetry plane) in order to examine the regions of separation induced by the spoiler. The camera was mounted outside the tunnel working section on the starboard side which was equipped with viewing windows. The laser sheet was directed from underneath the tunnel working section (Fig. 3b). Within this plane, image capturing was achieved using a 50 mm f/1.8D Nikon lens. PIV image processing settings were the same as before, allowing for 4 mm spatial resolution. The estimated uncertainty for velocity measurements was 2% of the freestream velocity.

III. Results and Discussion

A. Drag Force

Figure 4 shows the change in drag coefficient with flow control, normalized by the baseline drag coefficient such that data lying below the horizontal axis represents a drag reduction. Placing the spoiler closer to the beginning of the upswept section has caused a large increase in the drag coefficient, as much as 19% at $x'_s/c = 2.5\%$ for the $h/D = 5\%$ spoiler. At around mid-chord, $x'_s/c = 47.5\%$, the $h/D = 2.5\%$ spoiler shows almost no change in drag coefficient compared to the baseline. Placing the spoiler further downstream, the resulting drag penalty decreases gradually until drag reductions are achieved. The maximum drag reduction for both heights occur at $x'_s/c = 87.5\%$, with a reduction of approximately 5% compared to the baseline. Beyond this location, the magnitude of the drag reduction decreases towards the trailing-edge for both heights, with a drag reduction of approximately 3.5% for both heights at $x'_s/c = 97.5\%$. Beyond the optimum location $x'_s/c = 87.5\%$, the effect of spoiler height h/D on drag reduction is negligible. In light of the drag

data, the spoiler locations x'_s/c = 2.5%, 47.5% and 87.5% are discussed in detail in the following sections.

B. Pressure Measurements

Figure 5 presents the surface pressure contours for x'_s/c = 2.5%, 47.5%, and 87.5% locations along with the baseline case for comparison. These plots show a view directly looking at the upsweep surface, and corresponding spoiler locations are denoted by the horizontal red lines. The baseline pressure measurement (Fig. 5a) identifies the vortex footprint towards the edge of the elliptical upsweep, which exists until about x'/c = 60%. This vortex footprint is the reason for the vortex drag since it represents the lowest pressures acting on the upsweep surface due to the vortex. Further discussion regarding the same baseline flowfield can be found in Reference [9]. At x'_s/c = 2.5% (Fig. 5b), there exists a large region of low pressure downstream of the spoiler due to flow separation induced by the spoiler itself. A wider vortex footprint also exists when compared to the baseline. Placing the spoiler closer to the mid-chord of the upsweep, x'_s/c = 47.5% (Fig. 5c), appears to have caused a destruction in the vortex footprint to a certain extent. However, downstream of the spoiler, a region of low pressure is present across the span, although not as drastic as with the x'_s/c = 2.5% location.

Figure 5d presents the surface pressure measurements for the optimum location x'_s/c = 87.5%. For this drag reducing configuration, an increase in surface pressure is evident just upstream of the spoiler. Figure 6 presents the centerline (z = 0) pressure profiles for the same spoiler configurations compared with the baseline measurements. These identify the increase in pressure upstream of each spoiler location along with the low pressure separation region downstream of the spoiler. At the most upstream location x'_s/c = 2.5% (Fig. 6a), there exists a large low pressure region downstream of the spoiler, resulting in a large drag penalty. Closer to the mid-chord at x'_s/c = 47.5% (Fig. 6b), the low pressure region downstream of the spoiler is balanced to a certain extent by the increase in surface pressure ahead of the spoiler, resulting in a smaller drag penalty (or almost no drag penalty for the h/D = 2.5% height). At the optimum location, x'_s/c = 87.5% (Fig. 6c), there exists a large positive pressure ahead of the spoiler, which is larger in magnitude than for the previous locations, although this was not immediately apparent on the surface pressure distributions in Fig. 5d. Furthermore, due to the elliptical shape of the upsweep, there is a much

smaller surface area downstream of the spoiler for the low pressure separated flow to influence the drag. Flow physics for these configurations will be examined in the following sections.

C. Time-Averaged Flowfield

Figure 7 presents the time-averaged streamwise vorticity for the spoiler location x'_s/c = 2.5% along with the baseline flowfield for comparison. The results are presented as a three-dimensional perspective view with the flow approaching from right to left, the laser lines intersecting the model surface at each of the measurement locations are denoted by dotted lines.

For the baseline case (Fig. 7a), the vortex formation by the roll-up of the shear layer shed from the outboard edge of the afterbody is dominant at the first two measurement stations x/L = 0.2 and 0.4. An axisymmetric vortex core region starts appearing beyond the third measurement plane x/L = 0.6, which gradually starts to move away from the upsweep surface towards the trailing-edge where the fully developed vortex is present. Further details pertinent to this baseline flow can be found elsewhere [9].

For the x'_s/c = 2.5% location (Figs 7b and 7c), at the most upstream station (x/L = 0.2) the vortex formation occurs further outboard in comparison to the baseline due to the presence of flow separation immediately downstream of the spoiler. As the vortex approaches the trailing-edge it becomes increasingly diffused for both spoiler heights, with the vortex appearing more diffused for the larger spoiler height h/D = 5% (Fig. 7c). Figure 8 presents the time-averaged velocity and vorticity in the streamwise (z = 0) plane for the same spoiler location with flow approaching from left to right, and shows the large extent of flow separation due to the spoiler, contributing to its high drag penalty. The streamlines suggest that the flow reattaches at around mid-chord for both spoiler heights. The separated region appears to be a source of turbulence for the afterbody vortices and causes the vortices to become more diffused.

Figure 9 presents a three-dimensional perspective view of the time-averaged streamwise vorticity for the spoiler placed at x'_s/c = 47.5%. The first two measurement planes x/L = 0.2 and 0.4 for both spoiler heights show very similar flowfields compared to the baseline since the spoiler is located downstream of both these measurement planes. The first measurement plane downstream of the spoiler, x/L = 0.6, shows that the initial afterbody vortex is destroyed compared to the baseline flow. Remnants of the original vortex can still be seen, along with signs of a new afterbody vortex starting to form close to the surface. In-between these two vortices is a region of

vorticity with opposite sign, thought to be originating from the spoiler, more prominently observable in Fig. 9c for h/D = 5%. This interaction results in the formation of a very diffuse vortex structure towards the trailing-edge in comparison to the baseline case. The time-averaged velocity and vorticity in the streamwise (z = 0) plane in Fig. 10 show regions of flow separation for both spoiler heights, much less prominent than for the spoiler location x'_s/c = 2.5% seen in Fig. 8. Hence at this location, a smaller parasitic drag is expected due to the spoiler. For the h/D = 2.5% case, the parasitic drag has been compensated by the build up of high pressure ahead of the spoiler, leading to a drag coefficient almost equal to the baseline.

The three-dimensional perspective view of the time-averaged streamwise vorticity for the optimum location x'_s/c = 87.5% is shown in Fig. 11. At first glance there appears to be no appreciable change in vortex structure when the spoiler is placed at this location for both spoiler heights, with very similar time-averaged flowfields in comparison to the baseline case. However, the vortex at the trailing-edge appears to have been displaced away from the surface due to the presence of the spoiler, more observable in Fig. 11c with the larger height (h/D = 5%) spoiler. This effect will be discussed and quantified in the forthcoming discussion. The time-averaged velocity and vorticity in the streamwise (z = 0) plane are presented in Fig. 12, where a region of flow separation exists downstream of the spoiler. In this case, the low pressure region is close enough to the trailing-edge and the flow is deflected downward into the wake of the spoiler. This feature was not seen with the spoiler locations presented previously in Fig. 8 and Fig. 10, where the streamlines near the trailing-edge leave the model smoothly. For the optimal location of the spoiler, the effect is similar to the action of a Gurney flap placed on airfoils [22]. The suggested analogy is based on the deflection of the flow. A Gurney flap can be considered as a special case of trailing-edge flaps, with a flap angle of 90 degrees [23], where the flow deflection at the trailing-edge increases the lift. Similarly, a Gurney flap placed on the upper surface of an airfoil can be used to deflect the flow upwards to reduce the lift during gust encounters [24].

Having discussed the vortex characteristics using the time-averaged flowfields, it is desirable to quantify the strength of the vortex within each crossflow measurement plane. In order to assess the vortex strength, the circulation of each crossflow measurement plane was calculated using a numerical method in MATLAB®. The center of the vortex was located initially using the Q-criterion [25,26]. To calculate the Q-criterion, the velocity gradient tensor, ∇u, is first decomposed into symmetrical and asymmetrical components; the strain tensor, $S = 0.5(\nabla u + \nabla u^{T})$ and the

vorticity tensor, $\Omega = 0.5(\nabla u - \nabla u^T)$. A vortex is present in the region where $Q = 0.5(\|\Omega\|^2 - \|S\|^2) > 0$, and the center of the vortex is identified as the location of maximum Q value. The circulation within the immediate neighbourhood of this center was then calculated using an area integral of vorticity, before expanding the area outward along the grid by one spatial resolution unit and recalculating the circulation until the resulting change in circulation was less than 0.5%. The Q-criterion was considered a more robust method of locating the vortex center as opposed to using maximum vorticity since it is capable of separating regions of rotation from regions of strain which may have high vorticity if a shear layer is present. Determining the circulation using the current method overcomes the ambiguity of choosing an arbitrary domain of integration to perform the calculation, furthermore, the influence of background noise is minimal due to the enforced 0.5% change criterion.

The calculated circulation for the three spoiler locations are shown in Fig. 13. The baseline circulation increases rapidly between the x/L = 0.2 and 0.4 stations due to the strong shear layer present at these measurement planes, and keeps increasing towards the trailing-edge as vorticity is continuously shed into the vortex core. The shear layer is still present at the further downstream stations but is weak in comparison to the vortex and hence is not clearly visible in the time-averaged vorticity presented previously. With spoiler location at x'_s/c = 2.5% (Fig. 13a), the circulation growth is more rapid. At x/L = 0.6, for both spoiler heights, there is a larger circulation compared to the baseline and this value stays almost constant until x/L = 1.0, with the h/D = 2.5% and 5% heights resulting in an increased circulation by 6% and 13% compared to the baseline respectively. It is worthy noting that the rapid increase in vortex circulation (until x/L = 0.6) occurs while the flow in the z = 0 plane is separated (see Fig. 8). With the spoiler closer to the mid-chord at x'_s/c = 47.5% (Fig. 13b), the resulting growth in circulation is smaller in magnitude compared to the baseline at the most upstream measurement planes ahead of the spoiler (x/L = 0.2 and 0.4), with both spoiler heights showing equal values of circulation. Between the x/L = 0.4 and 0.6 measurement planes, there is a clear deceleration in the circulation growth due to the disruption of the shear layer by the spoiler at x'_s/c = 47.5%. Although there is some recovery at x/L = 0.8 due to the merging of the two vortices (see Fig. 9), the final circulation at the trailing-edge does not recover back to the baseline value. Hence placing the spoiler closer to the mid-chord of the upsweep has resulted in a slightly weaker afterbody vortex at the trailing-edge, with the h/D = 2.5% and 5% heights resulting in 4% and 8% lower circulations compared to the baseline

respectively. A weaker vortex at the trailing-edge is desirable, since it has been shown previously that the vortex strength at the trailing-edge can have direct implications on the overall drag coefficient [9]. However, with the spoiler at this location, this decrease in vortex strength was inadequate to result in a drag reduction due to the parasitic drag of the spoilers discussed previously.

The circulation for the optimum spoiler location x'_s/c = 87.5% is shown in Fig. 13c, and can be observed to be almost equal to the baseline circulation at most of the measurement stations for both spoiler heights. This was expected since the time-averaged flowfield encountered in Fig. 11 was very similar to the baseline. It was mentioned during the discussion for Fig. 11 that the vortex appeared to be displaced downwards away from the upsweep near the trailing-edge. In order to quantify this, the vortex centroid [27] location within the crossflow plane was obtained in the y-direction according to Equation 1:

$$\bar{y} = \frac{1}{\Gamma} \iint y\omega \, dydz \tag{1}$$

The first measurement station x/L = 0.2 was excluded from this analysis as the flow was dominated by the shear layer. Once the centroids were obtained, the distance of each centroid location from the surface of the model was calculated for the baseline ($\bar{H}_{ref}$) and flow control cases ($\bar{H}$) at each crossflow measurement plane. The difference of these two parameters ($\bar{H} - \bar{H}_{ref}$) represent a displacement of the vortex due to the flow control, with positive denoting the vortex displacing away from the surface at that particular measurement plane. The results for the spoiler location x'_s/c = 87.5% are presented in Fig. 14. At x/L = 0.4 and 0.6 the vortex is not displaced appreciably compared to the baseline centroid location, however, at x/L = 0.8 the vortex starts to be displaced away from the surface. At the trailing-edge x/L = 1.0, the vortex is clearly displaced away from the surface relative to the baseline vortex centroid, with the larger height h/D = 5% spoiler displacing the vortex further away from the surface compared to the h/D = 2.5% spoiler. Such a movement of the vortex away from the surface is desirable, since its influence on the surface pressure is reduced. This is one of the flow control strategies for tip/edge vortices as recently discussed [28].

D. Unsteady Aspects

Figure 15 presents three-dimensional views of the standard deviation of the velocity in the crossflow planes for the spoiler locations discussed previously, along with the baseline case for comparison. This represents the turbulence intensity within the flowfield, and is useful in visualizing unsteady flow features. Only the larger height h/D = 5% cases are presented since the h/D = 2.5% cases were qualitatively similar. For the baseline case in Fig. 15a, high levels of standard deviation are observed in regions where vortex roll-up and meandering occur. The shear layer that was not visible downstream of x/L = 0.6 in the time-averaged flow is now visible due to the flow unsteadiness. With the spoiler placed at x'_s/c = 2.5% (Fig. 15b), the highly unsteady flow generated by the spoiler is visible at the first three measurement planes from x/L = 0.2 to x/L = 0.6. Towards x/L = 0.8 and 1.0, the magnitude of the unsteadiness decreases since the flow is now reattached to the surface. The resulting vortex has ingested the turbulence generated from the spoiler, resulting in a large region of unsteadiness at the final two measurement stations which caused an apparent diffusion of the time-averaged vorticity observed previously (Fig. 7).

For the spoiler placed at x'_s/c = 47.5% (Fig. 15c) the first measurement plane x/L = 0.2 looks very similar to the baseline since the effect of the spoiler is not felt at this location. At x/L = 0.4, there appears to have been a reduction in the peak unsteadiness closer to the vortex core location, with an increased unsteadiness towards the centerline as the flow approaches the spoiler location. Downstream of the spoiler at x/L = 0.6, the turbulent wake of the spoiler is visible. Beyond this location, similar to the spoiler at x'_s/c = 2.5%, the vortex ingests the turbulence as seen between x/L = 0.8 and 1.0, resulting in an increase in its meandering and appearing highly diffuse in the time-averaged sense (Fig. 9). For the x'_s/c = 87.5% spoiler location (Fig. 15d), the unsteadiness appears very similar to the baseline for all measurement planes up to x/L = 0.8. The final measurement plane at the trailing edge, x/L = 1.0, shows the turbulence generated by the spoiler at this location. The displacement of the vortex away from the surface is also visible with the vortex core unsteadiness located further away from the surface in comparison to the baseline case.

E. Upstream Vortex Generators

The results so far suggest that manipulation of the afterbody vortices (displacing them away from the surface, diffusing them by turbulence ingestion, reducing their circulation, etc.) may be useful for drag reduction, however this is counteracted by the enhanced negative pressures due to

the spoiler-induced flow separation. In an effort to manipulate the afterbody vortices without the use of mini-spoliers, we investigated the possibility of generating smaller vortices and letting them interact with the afterbody vortices. We used vortex generators (VGs) near the origin of the afterbody vortices as shown in the examples in Figure 16. The VGs studied were of half delta wing (or vane) type, which were preferred over rectangular plate designs due to the expected high VG incidence angles without compromising flow quality. The chord length was fixed at c_{VG}/D = 27.5%, and the half delta wing VG tested had a leading edge sweep Λ = 70°, resulting in a VG height to model diameter ratio of h_{VG}/D = 10%. The locations of the VG pairs were varied along the side edges of the circular fuselage on the afterbody on both sides of the model, such that the VG trailing edges were placed (when viewed from a sideview) at x/c = 5%, 10%, (and with spacings of x/c = 10% from there on) up to x/c = 50% along the afterbody. At each location, the effect of changing the VG incidence angle was investigated for β = 20°, 30° and 40°, relative to the freestream direction. VG configurations are usually characterized based on whether a pair are co-rotating or counter-rotating relative to each other [29,30]. However, in the current study, the VGs are characterized based on the rotational sense of the generated vortex in comparison to the afterbody vortex. Drag force data revealed that the best location with drag reduction potential was x/c = 20% for a co-rotating VG pair with β = 20°. At this configuration, the drag coefficient was equal to the baseline. This suggested that there is an underlying flow mechanism that overcomes the parasitic drag of the VG. The same was not true for the counter-rotating case, which resulted in a drag increase. PIV measurements were performed for this VG location (x/c = 20%) and incidence angle (β = 20°) for both co-rotating (beneficial) and counter-rotating (detrimental) cases in order to understand the flow interactions.

Figure 16 presents the three-dimensional perspective views of time-averaged vorticity for the VG cases. For the co-rotating configuration in Fig. 16b, the co-rotating vortex from the VG is captured at the x/L = 0.4 measurement plane, and is seen to interact with the afterbody vortex at this location, distorting its time-averaged vorticity compared to the baseline. Further downstream, these two vortices appear to merge together and form a diffused vortex at the trailing-edge, which appears to be further away from the surface compared to the baseline time-averaged vortex. The counter-rotating VG configuration is presented in Fig. 16c, where the counter-rotating vortex generated by the VG is visible at the x/L = 0.4 and 0.6 locations. However, the afterbody vortex flow has not changed significantly in comparison to the baseline. The time-averaged vortex that

exists at the trailing-edge, x/L = 1.0, appears very similar to that of the baseline case. The circulation was calculated for all measurement planes using the same method discussed previously. It was found that the growth in circulation was more rapid for the counter-rotating VG, and slower for the co-rotating VG compared to the baseline. However, the circulation for the fully developed vortex at the trailing-edge recovered back to baseline values for both cases. The vortex centroid locations were calculated using the same methods described previously for measurement planes downstream of x/L = 0.4 for both VG configurations, and are presented in Fig. 17. It can be observed that the vortex centroid has been displaced away from the surface in comparison to the baseline for the co-rotating case at all measurement locations. This movement of the vortex away from the surface is the reason for a resulting drag coefficient equal to the baseline, with the parasitic drag of the VG being compensated by the movement of the vortex away from the surface, especially at upstream locations where the vortex influence on the surface pressure is the largest (e.g. x/L = 0.4). In contrast, the counter-rotating case reveals that the centroids have moved closer to the surface, resulting in larger suction on the surface and larger drag penalty.

IV. Conclusions

The efficacy of the mini-spoilers for afterbody base drag reduction has been studied experimentally in a wind tunnel at a Reynolds number Re_D = 200,000 on a slanted base cylindrical model with a Φ = 28° upsweep angle. It was found that placing the spoilers closer to the beginning of the slanted section created a drag increase due to flow separation downstream of the spoiler, even though diffused vortices formed further downstream. The diffusion of the time-averaged vortex was due to the ingestion of turbulence emanating from the spoiler. Placing the spoiler closer to the mid-chord at x'_s/c = 47.5% resulted in the disintegration of the afterbody vortex and the formation of a new weaker vortex further downstream; however, drag reduction was not achieved at this location due to the parasitic drag of the spoiler. Drag reduction was achieved by moving the spoiler location further downstream. At the optimum location for drag reduction, x'_s/c = 87.5%, the spoiler heights h/D = 2.5% and 5% led to approximately 5% drag reduction. The structure of the afterbody vortex was unaffected, however the vortex was displaced away from the surface. The mini-spolier acts similar to a Gurney flap and deflects the flow and the afterbody vortices away from the surface. The same flow mechanism is observed when smaller co-rotating vortices are introduced to manipulate the trajectory of the afterbody vortices. The latter approach eliminates

the spoiler-induced separation, however it requires further optimization to reduce the drag due to the vortex generator itself.

Acknowledgments

This work was supported by the Air Force Office of Scientific Research, Air Force Material Command, USAF, under Grant Number FA9550-14-1-0126, monitored by Dr. Douglas Smith.

References

[1] Epstein, R. J., Carbonaro, M. C., and Caudron, F., "Experimental Investigation of the Flowfield about an Upswept Afterbody", *Journal of Aircraft*, Vol. 31, No. 6, 1994, pp. 1281-1290, doi: 10.2514/3.46648.

[2] Carter, D. L., and Givogue G., "Legacy Transport Aircraft Drag Reduction Overview", AIAA-2017-4225, *35th AIAA Applied Aerodynamics Conference*, 5-9th June 2017, Denver, CO, USA, doi: 10.2514/6.2017-4225.

[3] Bury, Y., Jardin, T., and Klockner, A., "Experimental Investigation of the Vortical Activity in the Close Wake of a Simplified Military Transport Aircraft", *Experiments in Fluids*, Vol. 54, No. 5, 2013, Article number 1524, doi: 10.1007/s00348-013-1524-4.

[4] Morel, T., "Effect of Base Slant on Flow in the Near Wake of an Axisymmetric Cylinder", *Aeronautical Quarterly*, Vol. 31, No. 2, 1980, pp. 132-147, doi: 10.1017/S0001925900010957.

[5] Maull, D. J., "The Drag of Slant-Based Bodies of Revolution", *The Aeronautical Journal*, Vol. 84, 1980, pp. 164-166, doi: 10.1017/S0001924000030955.

[6] Xia, X. J., and Bearman, P. W., "Experimental Investigation of the Wake of an Axisymmetric Body with a Slanted Base", *Aeronautical Quarterly*, Vol. 34, No. 1, 1983, pp. 24-45, doi: 10.1017/S0001925900009574.

[7] Britcher, C. P., and Alcorn, C. W., "Interference-Free Measurements of the Subsonic Aerodynamics of Slanted-Base Ogive Cylinders", *AIAA Journal*, Vol. 29, No. 4, 1991, pp. 520-525, doi: 10.2514/3.10614.

[8] Bearman, P. W., "Review – Bluff Body Flows Applicable to Vehicle Aerodynamics", *Journal of Fluids Engineering, Transactions of the ASME*, Vol. 102, No. 3, 1980, pp. 265-274, doi: 10.1115/1.3240679.

[9] Bulathsinghala, D. S., Jackson, R., Wang, Z., and Gursul, I., "Afterbody Vortices of Axisymmetric Cylinders with a Slanted Base", *Experiments in Fluids*, 58:60, 2017. Article number 60, doi 10.1007/s00348-017-2343-9.

[10] Jackson, R., Wang, Z., and Gursul, I., "Control of Afterbody Vortices by Blowing", AIAA-2015-2777, *45th AIAA Fluid Dynamics Conference*, 22-26 June 2015, Dallas, TX, USA, doi: 10.2514/6.2015-2777.

[11] McCluney, B., and Marshall, J., "Drag Development of Belfast", *Aircraft Engineering*, Vol. 39, No. 10, 1967, pp. 33-37, doi: 10.1108/eb034302.

[12] Calarese, W., Crisler, W. P. & Gustafson, G. L., "Afterbody Drag Reduction by Vortex Generators", AIAA-1985-0354, *23rd AIAA Aerospace Sciences Meeting*, 1985, Reno, NV, USA, doi: 10.2514/6.1985-354.

[13] Wortmann, A., "Reduction of Fuselage Form Drag by Vortex Flows", *Journal of Aircraft*, Vol 36, No. 3, 1999, pp. 501-506, doi: 10.2514/2.2484.

[14] Smith, B. R., Yagle, P. J. & Hooker, J. R., "Reduction of Aft Fuselage Drag on the C-130 Using Microvanes", AIAA-2013-0105, *51st AIAA Aerospace Sciences Meeting*, 7-10 January 2013, Grapevine, TX, USA, doi: 10.2514/6.2013-105.

[15] Telli, H., Ayan, E., Soyer, S., Gülsever, E., and Özcan, S., "An Investigation of C-130 Aircraft Base Drag Reduction with Aftbody Modifications," AIAA-2016-3430, *34th AIAA Applied Aerodynamics Conference*, 13-17 June 2016, Washington, DC, USA, doi: 10.2514/6.2016-3430.

[16] McIlwain, S., Carter, D. L., Givogue, G., Lorang, T., Polito, R., Pereira, J., and Clark, C., "C-17 Globemaster III Vortex Control Finlets Simulation and Wind Tunnel Testing", AIAA-2017-4227, *35th AIAA Applied Aerodynamics Conference*, 5-9th June 2017, Denver, CO, USA, doi: 10.2514/6.2017-4227.

[17] Jackson, R., Wang, Z., and Gursul, I., "Afterbody Drag Reduction Using Active Flow Control", AIAA-2017-0954, *55th AIAA Aerospace Sciences Meeting*, January 2017, Grapevine, TX, USA, doi: 10.2514/6.2017-0954.

[18] Ahmed, S. R., Ramm, G., and Fatlin, G., "Some Salient Features of the Time-Averaged Ground Vehicle Wake", *SAE technical paper series*, 1984, No. 840300, doi: 10.4271/840300.

[19] Beaudoin, J. F., and Aider, J. L., "Drag and Lift Reduction of a 3D Bluff Body Using Flaps", *Experiments in Fluids*, Vol. 44, No. 4, 2008, pp. 491-501, doi: 10.1007/s00348-007-0392-1.

[20] Fourrie, G., Keirsbulck, L., Labraga, L., and Gillieron, P., "Bluff-Body Drag Reduction Using a Deflector", *Experiments in Fluids*, Vol. 50, No. 2, 2011, pp. 385-395, doi: 10.1007/s00348-010-0937-6.

[21] Moffat, R. J., "Describing the Uncertainties in Experimental Results", *Experimental Thermal and Fluid Science*, Vol. 1, No. 1, 1988, pp. 3-17, doi: 10.1016/0894-1777(88)90043-X.

[22] Wang, J.J., Li, Y.C. and Choi, K.-S., "Gurney Flap – Lift Enhancement, Mechanisms and Applications", *Progress in Aerospace Sciences*, vol. 44, 2008, pp. 22-47, doi: 10.1016/j.paerosci.2007.10.001.

[23] Liu, T. and Montefort, J., "Thin-Airfoil Theoretical Interpretation for Gurney Flap Lift Enhancement", *Journal of Aircraft*, vol. 44, no. 2, 2007, pp. 667-671. https://arc.aiaa.org/doi/pdf/10.2514/1.27680

[24] Heathcote, D. J., Gursul. I, and Cleaver, D. J., "Aerodynamic Load Alleviation Using Mini-tabs", *Journal of Aircraft*, in print.

[25] Hunt, J. C. R., Wray, A. A., and Moin, P., "Eddies, Stream and Convergence Zones in Turbulent Flows", *Center for Turbulence Research Report CTR-S88*, Vol. 193, 1988.

[26] Jeong, J., and Hussain, F., "On the Identification of a Vortex", *Journal of Fluid Mechanics*, Vol. 285, 1995, pp. 69-94, doi: 10.1017/S0022112095000462.

[27] Leweke, T., Le Dizés, S., and Williamson, C. H. K., "Dynamics and Instabilities of Vortex Pairs", *Annual Reviews of Fluid Mechanics*, Vol. 48, 2016, pp. 507-541, doi: 10.1146/annurev-fluid-122414-034558.

[28] Gursul, I. and Wang, Z., "Flow Control of Tip/Edge Vortices", *AIAA Journal*, Special Issue on Flow Control, in print, doi: 10.2514/1.J056586.

[29] Lin, J. C., "Review of Research on Low-Profile Vortex Generators to Control Boundary-Layer Separation", *Progress in Aerospace Sciences*, Vol. 38, No. 4-5, 2002, pp. 389-420, doi: 10.1016/S0376-0421(02)00010-6.

[30] Ashill, P. R., Fulker, J. L., and Hackett, K. C., "A Review of Recent Developments in Flow Control", *The Aeronautical Journal*, Vol. 109, No. 1095, 2005, pp. 205-232, doi: 10.1017/S0001924000005200.

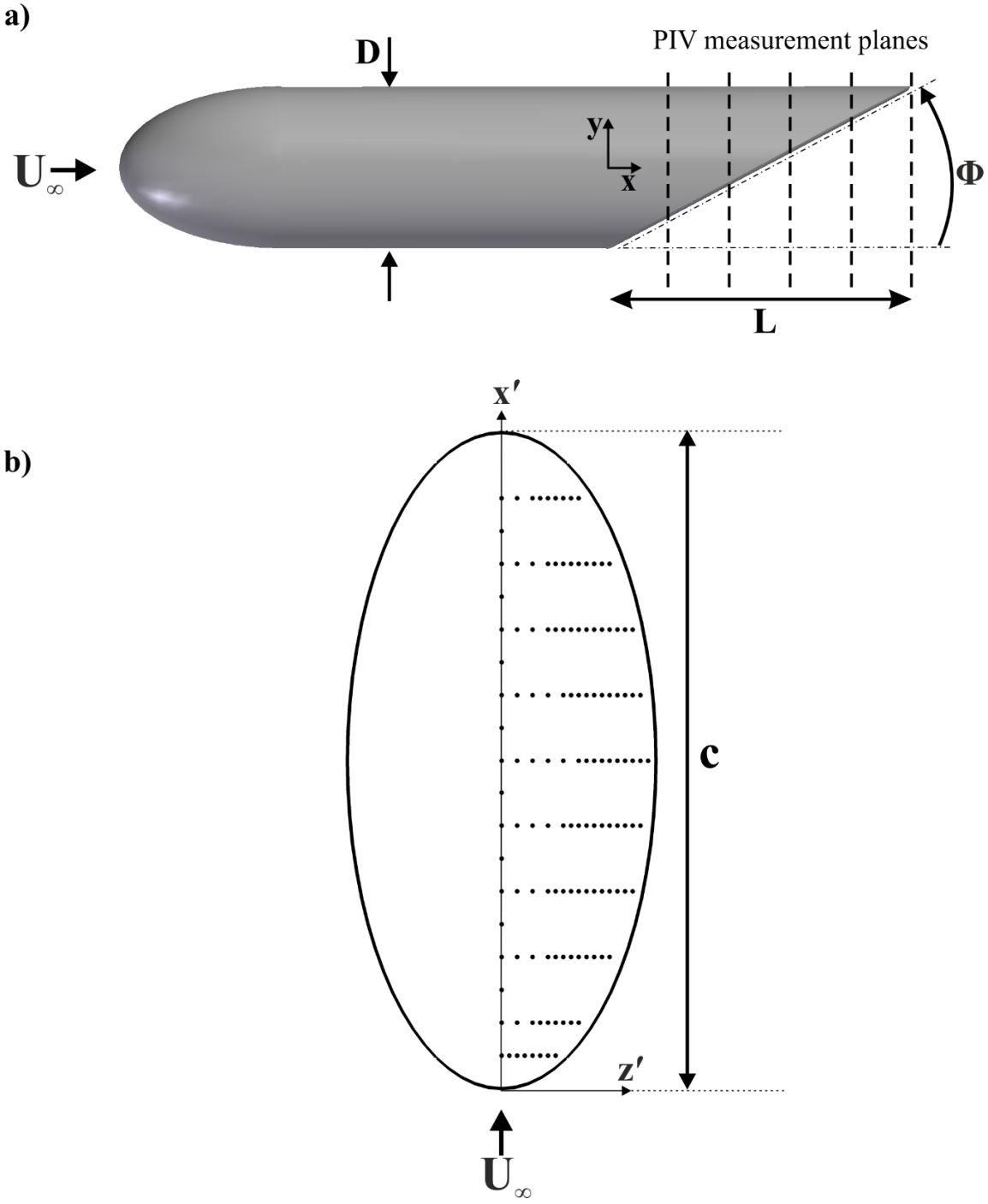

Figure 1: a) Model parameters and PIV crossflow measurement planes, b) pressure tap locations on upswept surface.

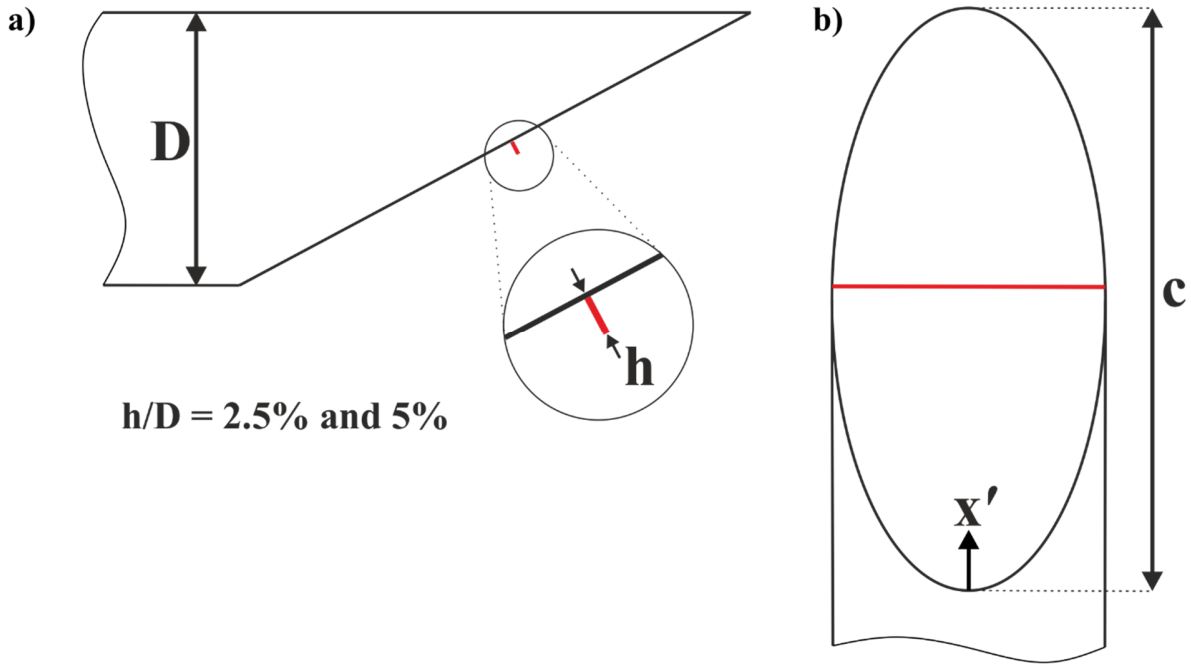

Figure 2: Schematic of mini-spoilers placed on the model: a) view from port side, b) view looking at upsweep surface.

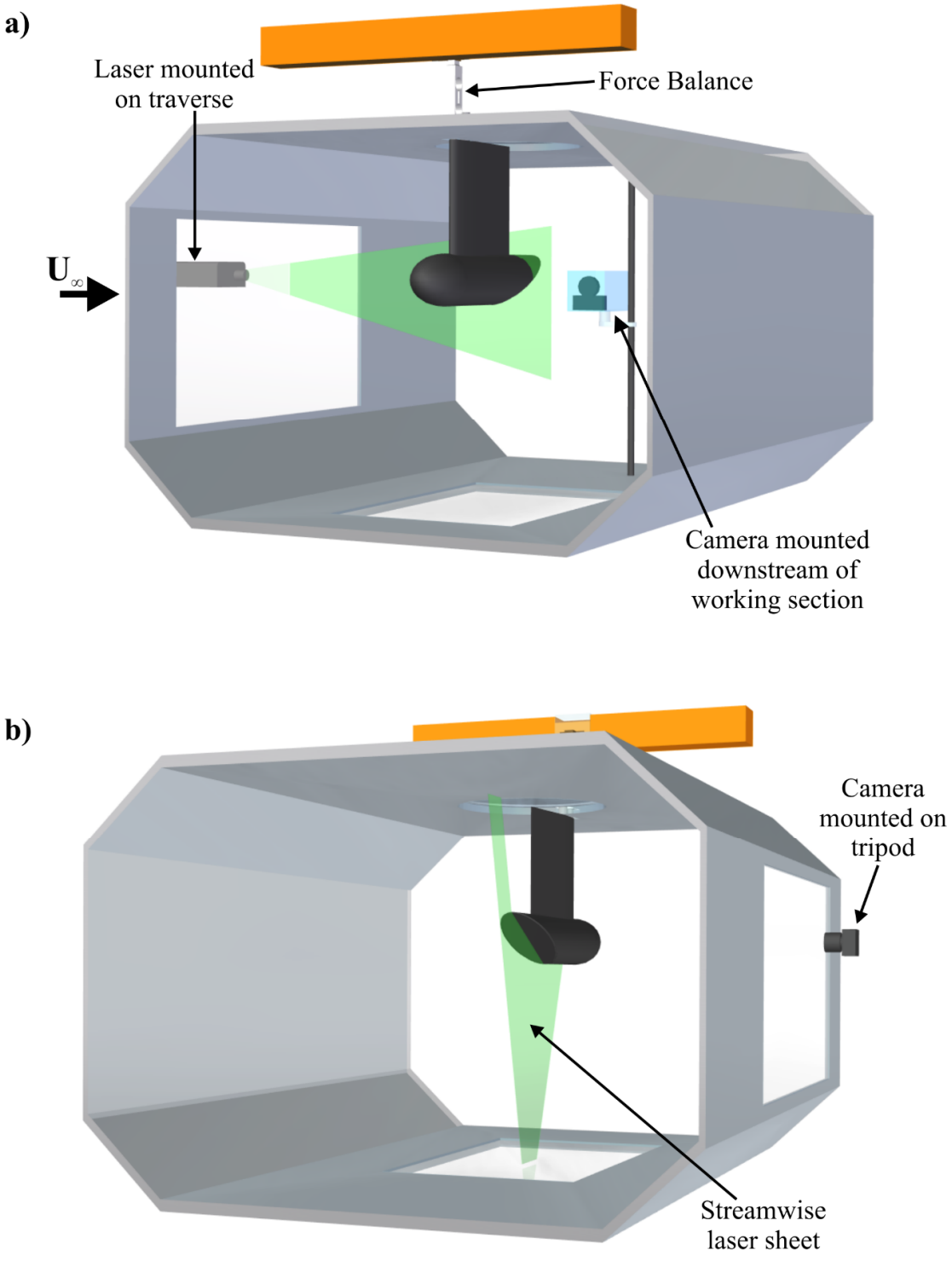

Figure 3: PIV setup for measurements in a) crossflow plane, b) streamwise (z = 0) plane.

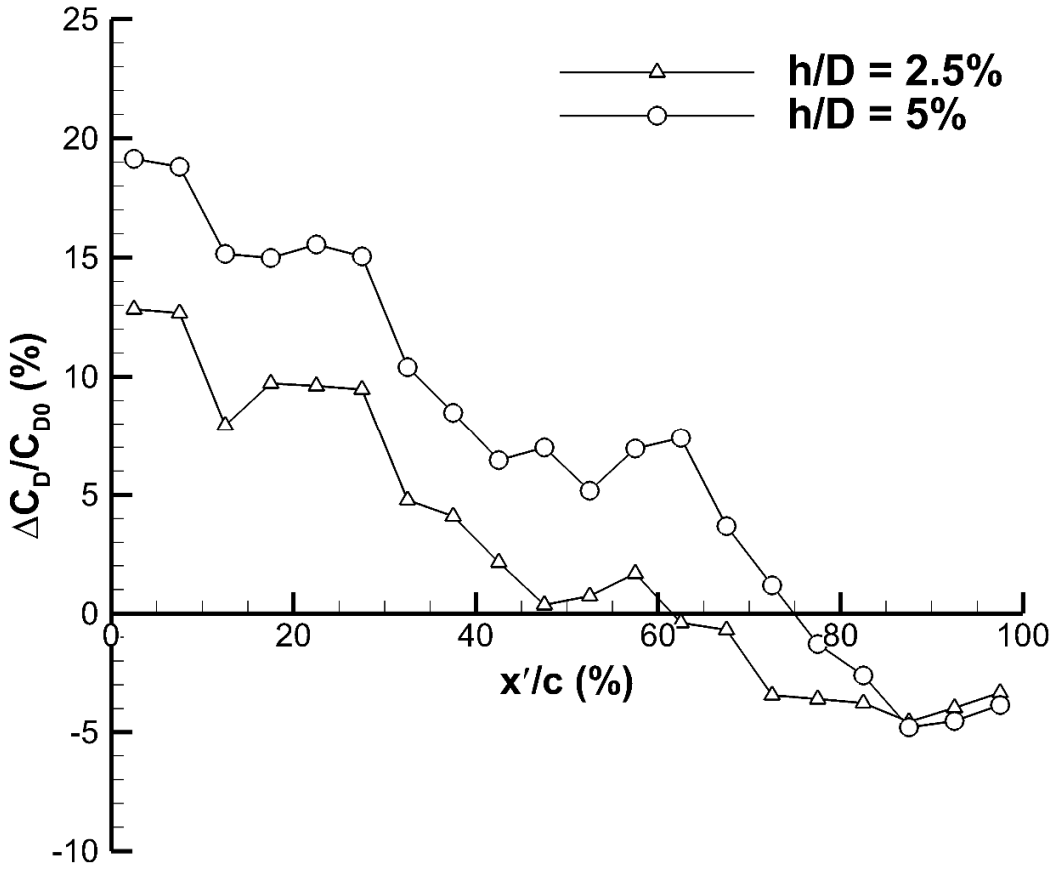

Figure 4: Variation of change in drag coefficient with spoiler location.

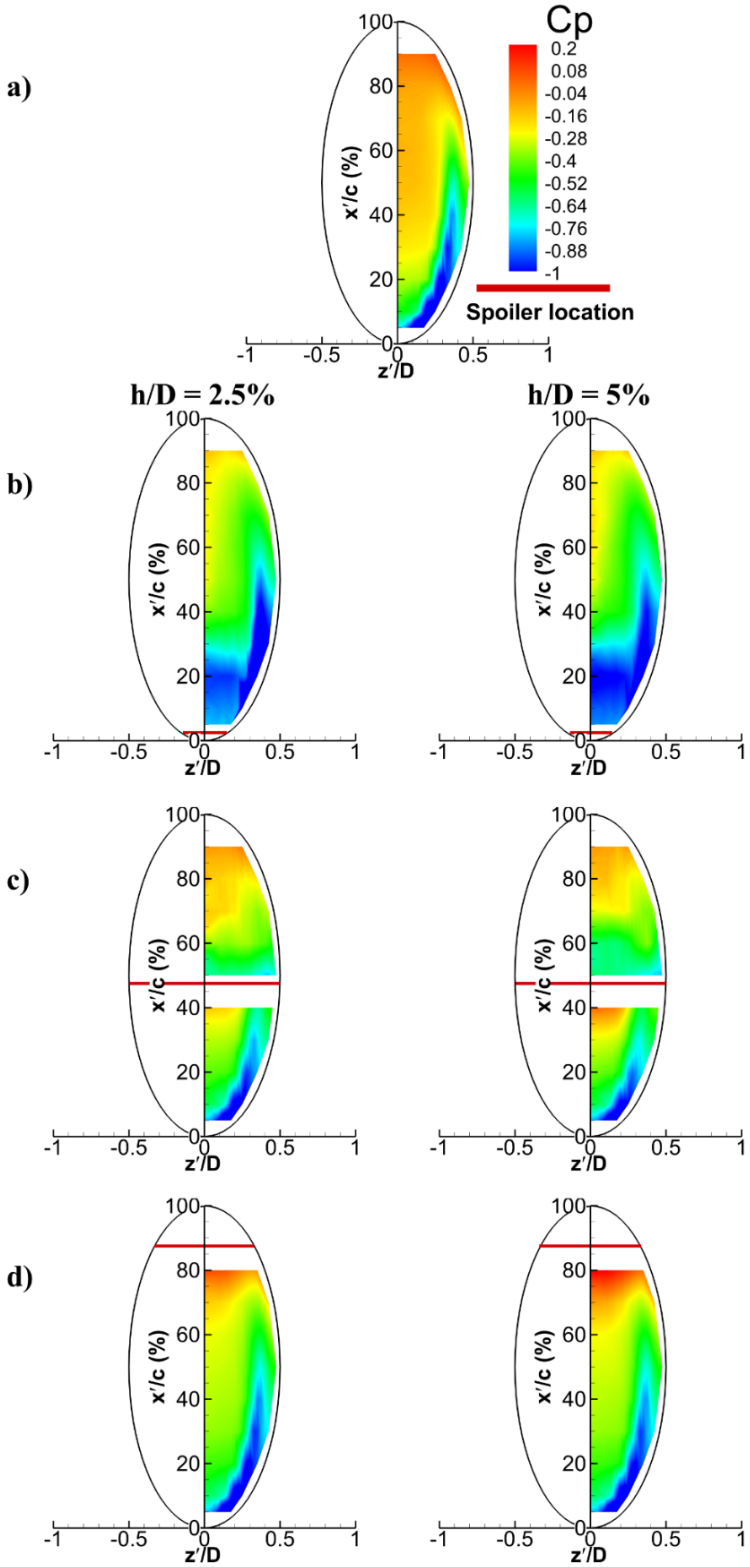

Figure 5: Surface pressure distributions for (a) baseline case; and selected spoiler locations, *h/D* = 2.5% (left) and *h/D* = 5% (right): b) x'_s/c = 2.5%, c) x'_s/c = 47.5% and d) x'_s/c = 87.5%. Spoiler locations are denoted by horizontal red lines.

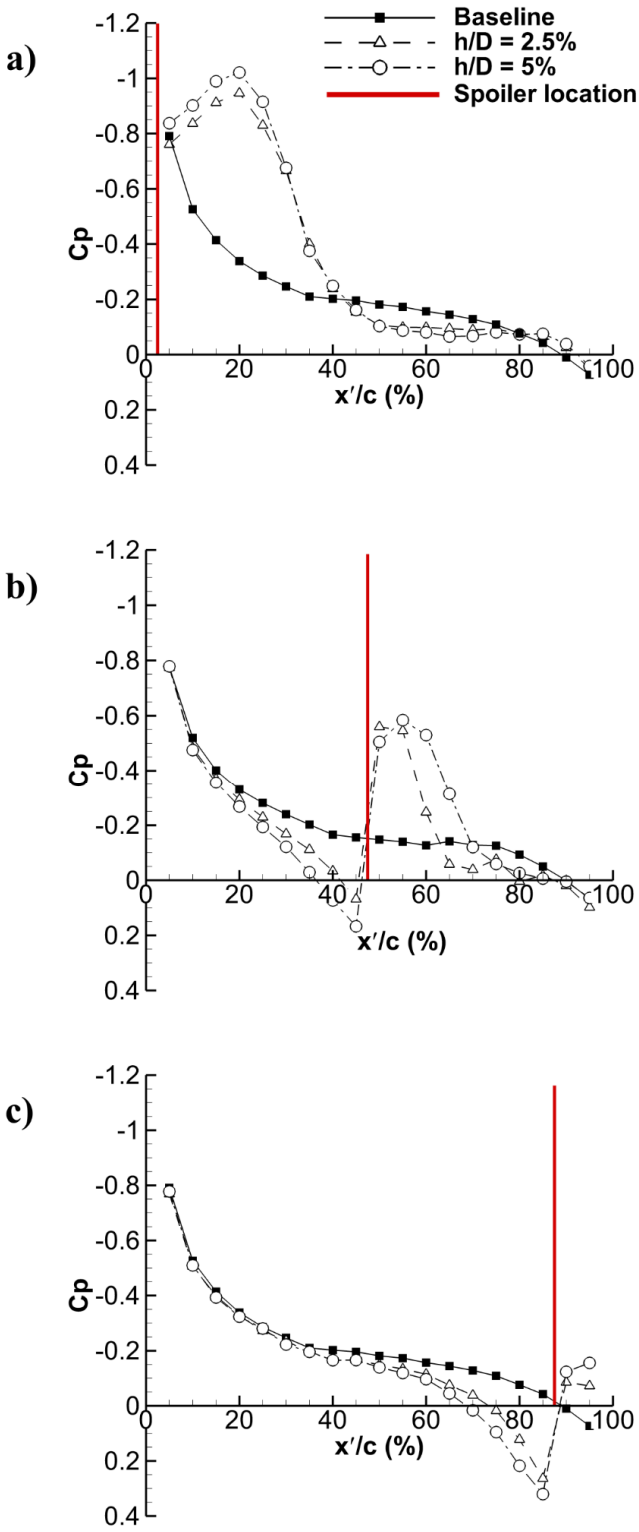

Figure 6: Centerline (z = 0) pressure distribution for a) x'_s/c = 2.5%, b) x'_s/c = 47.5% and c) x'_s/c = 87.5%. Spoiler locations are denoted by vertical red lines on each plot.

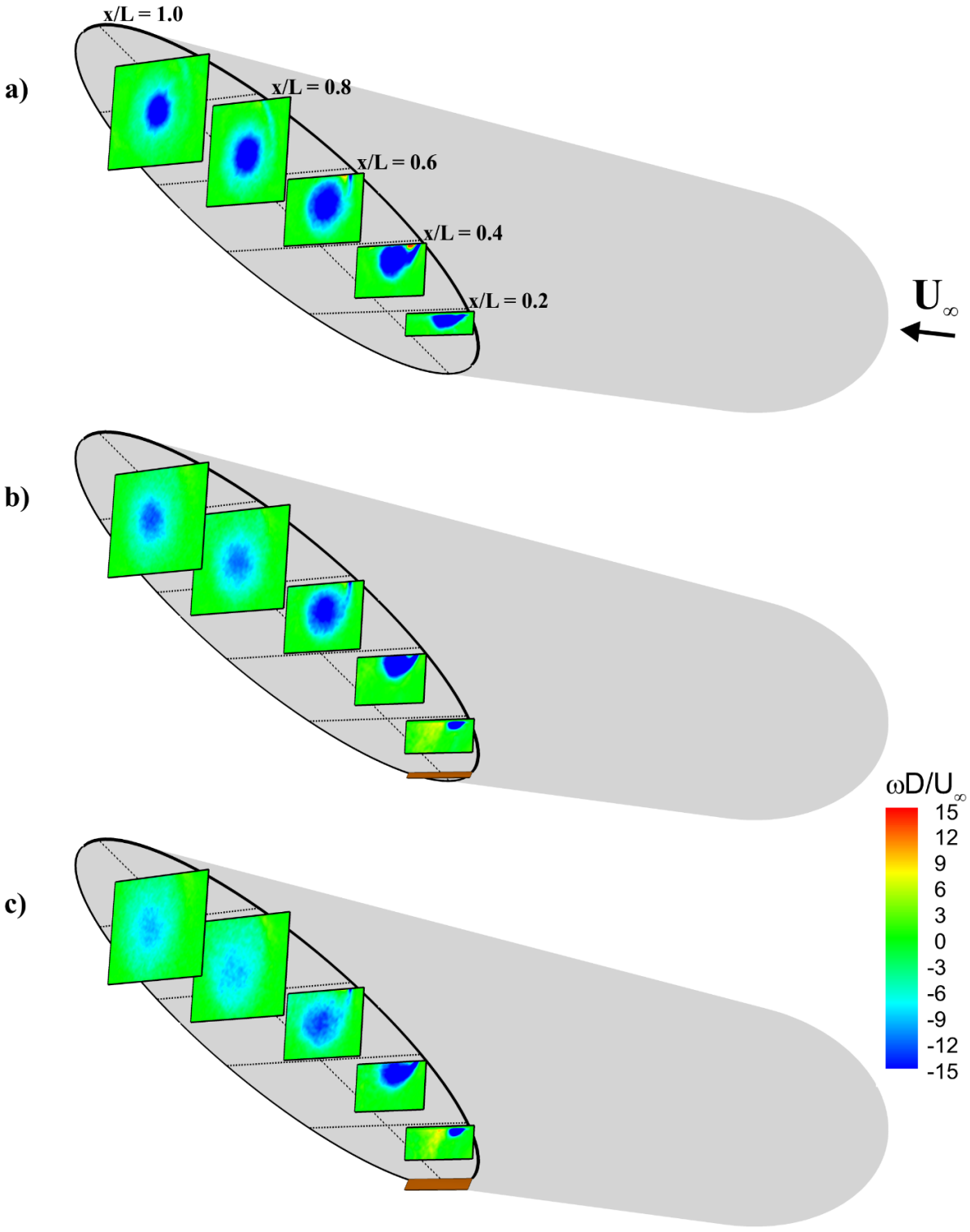

Figure 7: Three-dimensional perspective view of time-averaged vorticity for a) baseline case; and spoiler location x'_s/c = 2.5%, b) h/D = 2.5% and c) h/D = 5%.

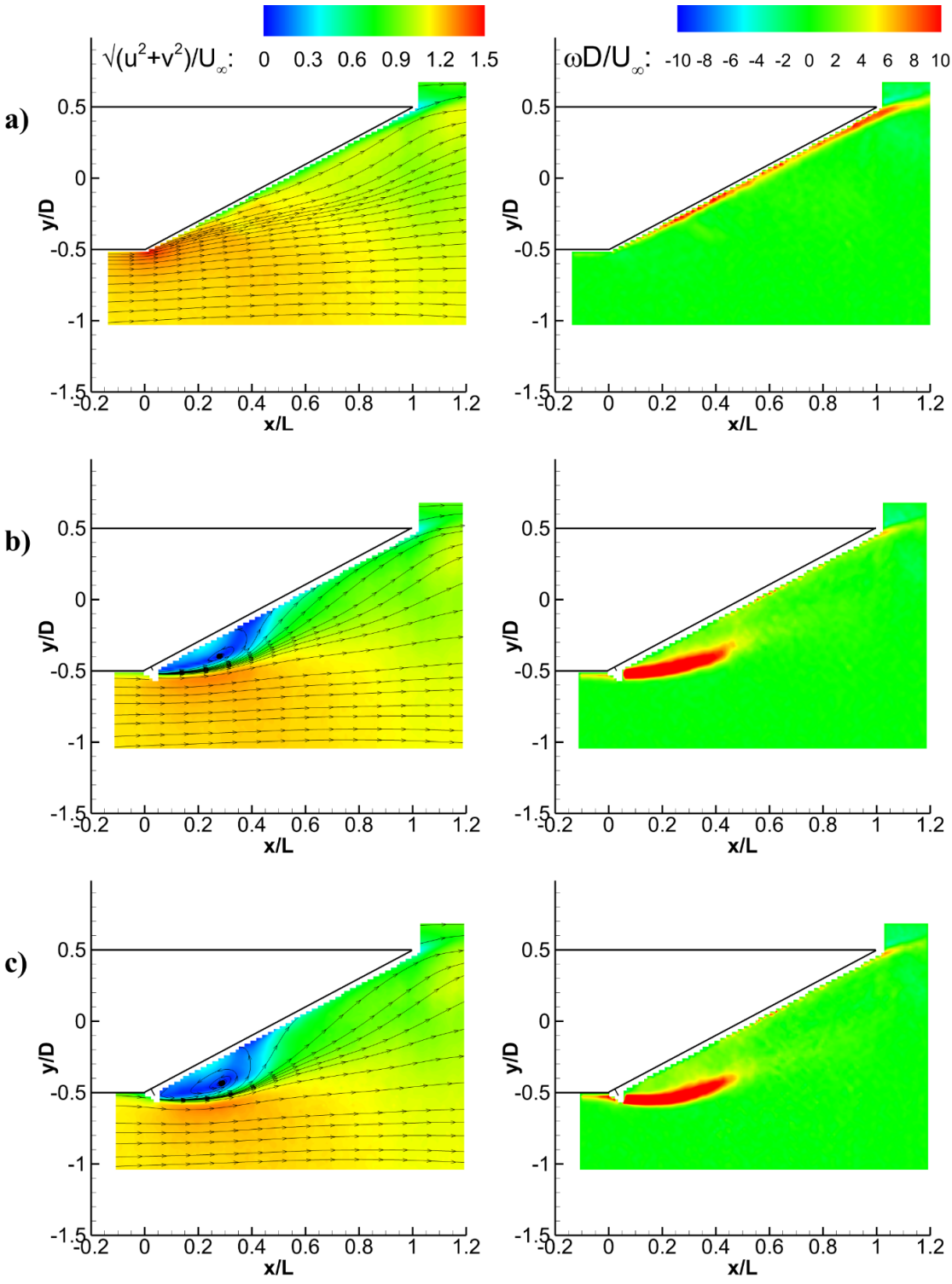

Figure 8: Time-averaged normalized velocity magnitude (left) and vorticity (right) on the *z*=0 plane for a) baseline case; and spoiler placed at x'_s/c = 2.5%, b) *h/D* = 2.5% and c) *h/D* = 5%.

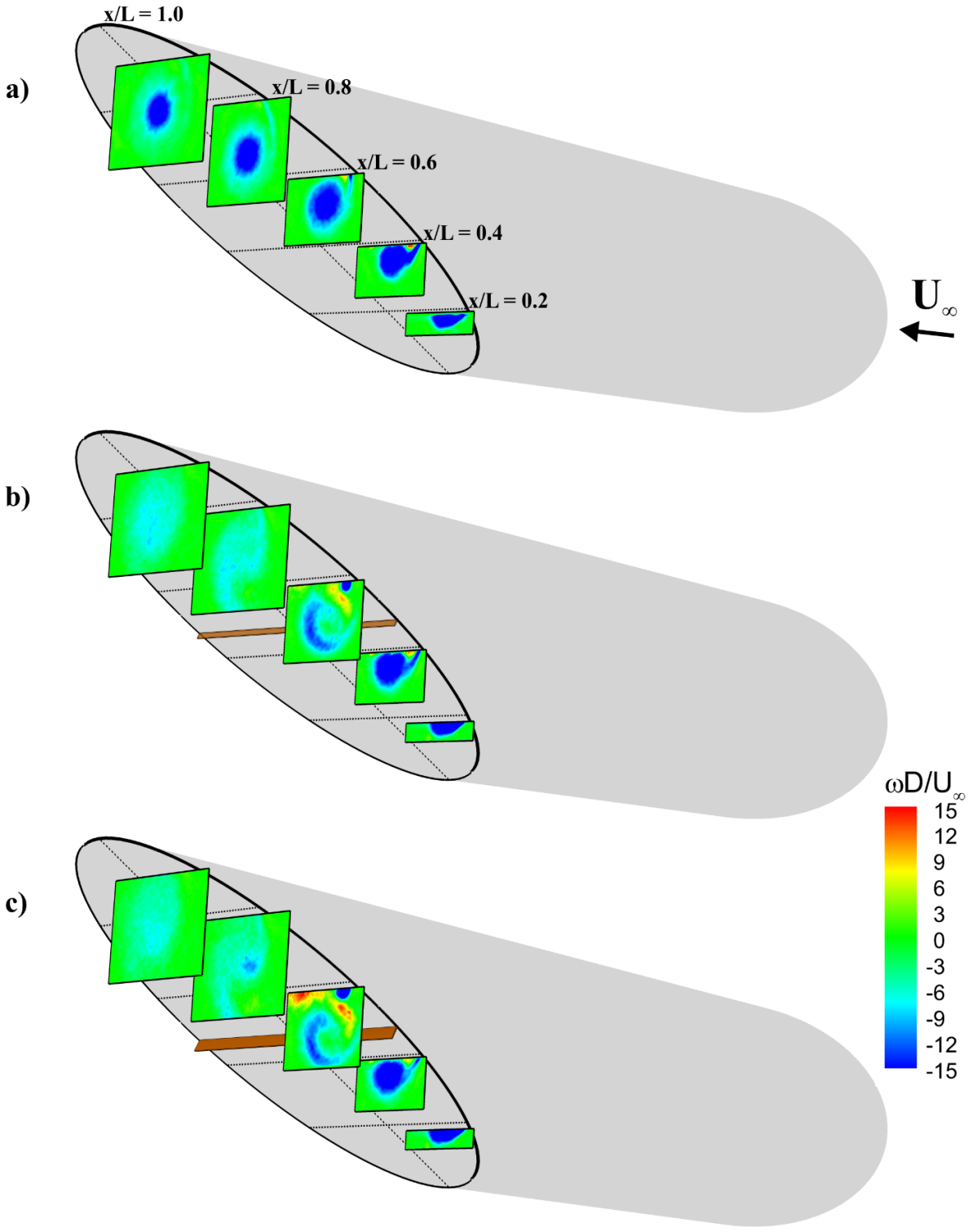

Figure 9: Three-dimensional perspective view of time-averaged vorticity for a) baseline case; and spoiler placed at x'_s/c = 47.5%, b) h/D = 2.5% and c) h/D = 5%.

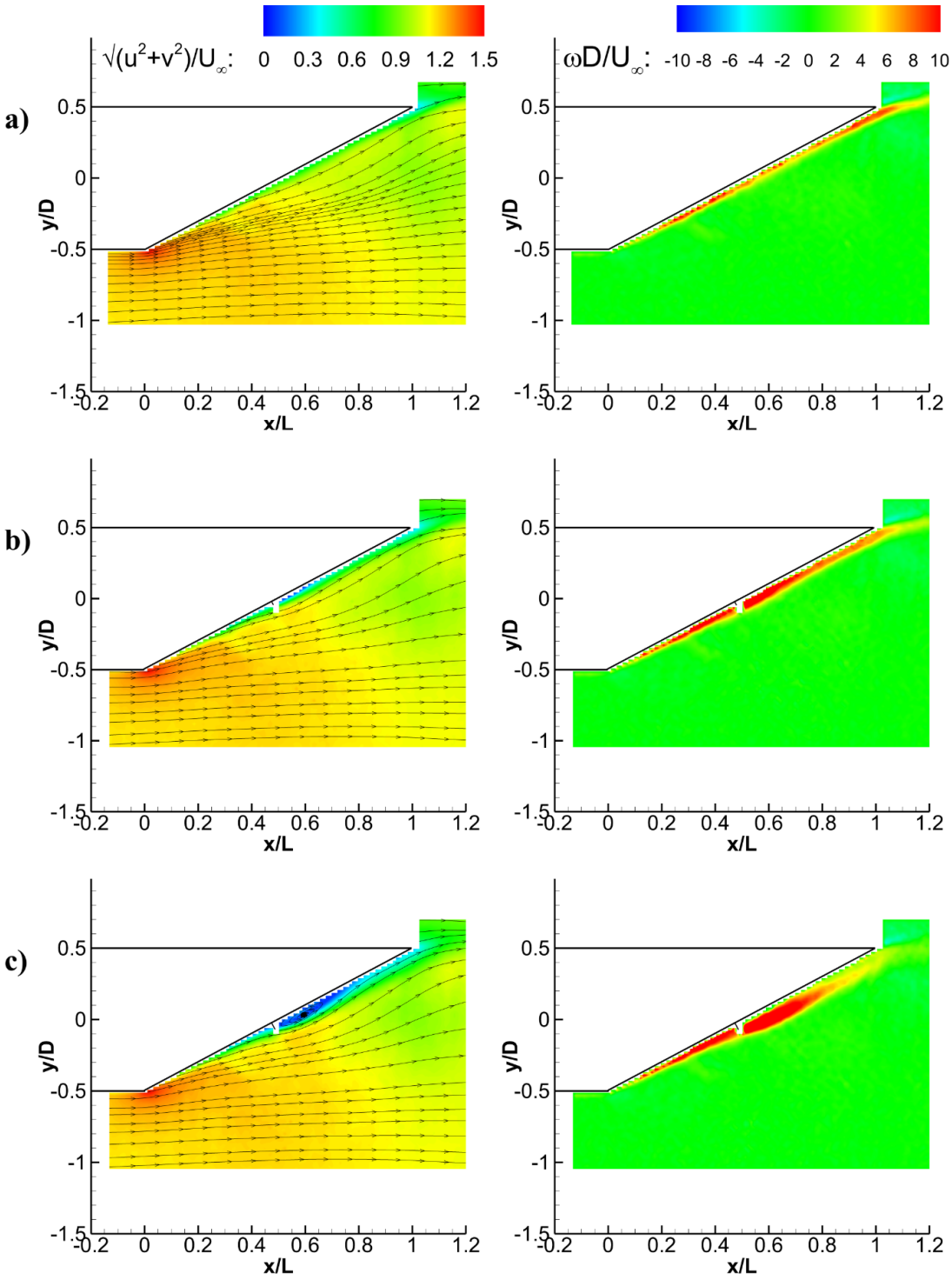

Figure 10: Time-averaged normalized velocity magnitude (left) and vorticity (right) on the *z*=0 plane for a) baseline case; and spoiler placed at x'_s/c = 47.5%, b) *h/D* = 2.5% and c) *h/D* = 5%.

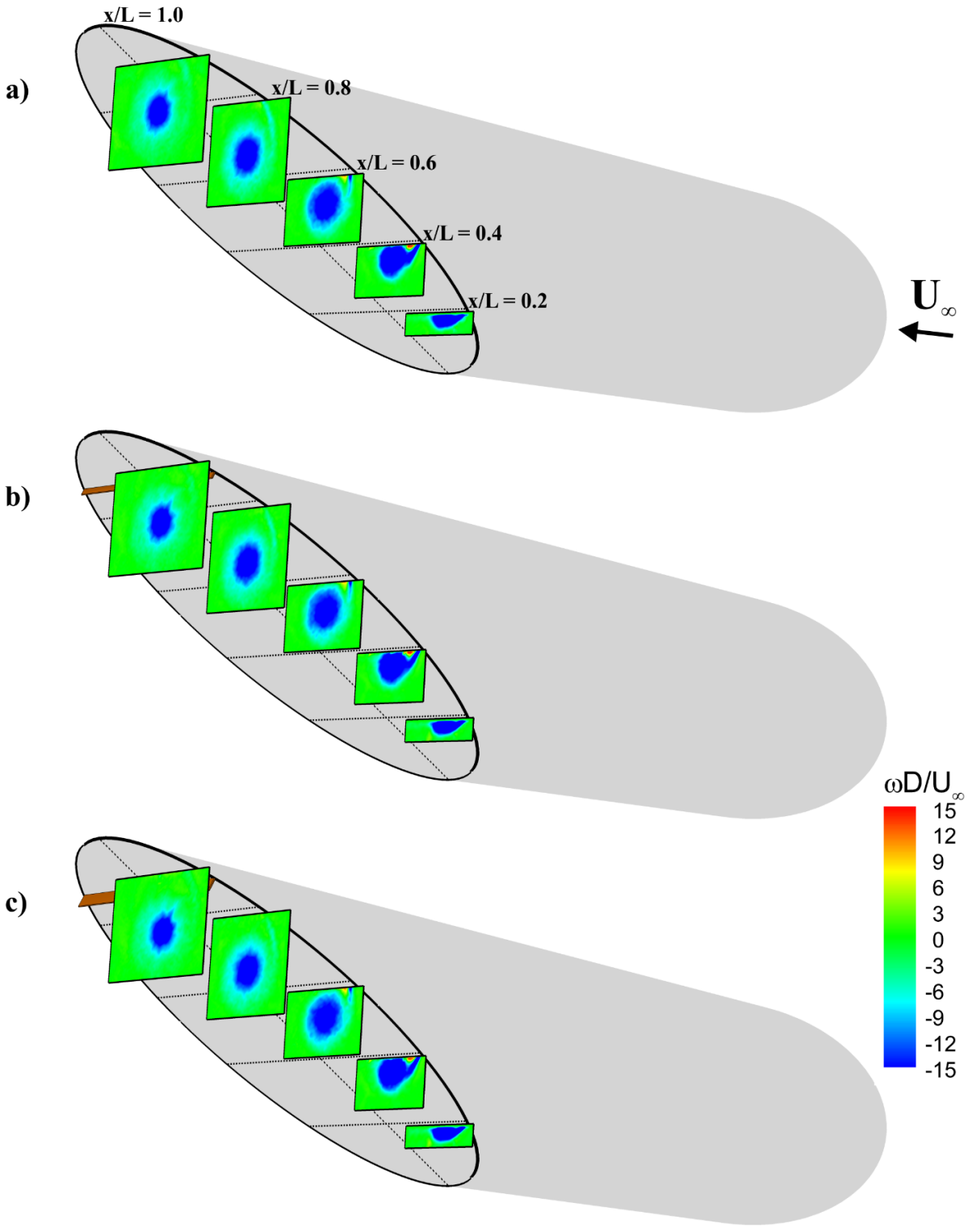

Figure 11: Three-dimensional perspective view of time-averaged vorticity for a) baseline case; and spoiler placed at x'_s/c = 87.5%, b) h/D = 2.5% and c) h/D = 5%.

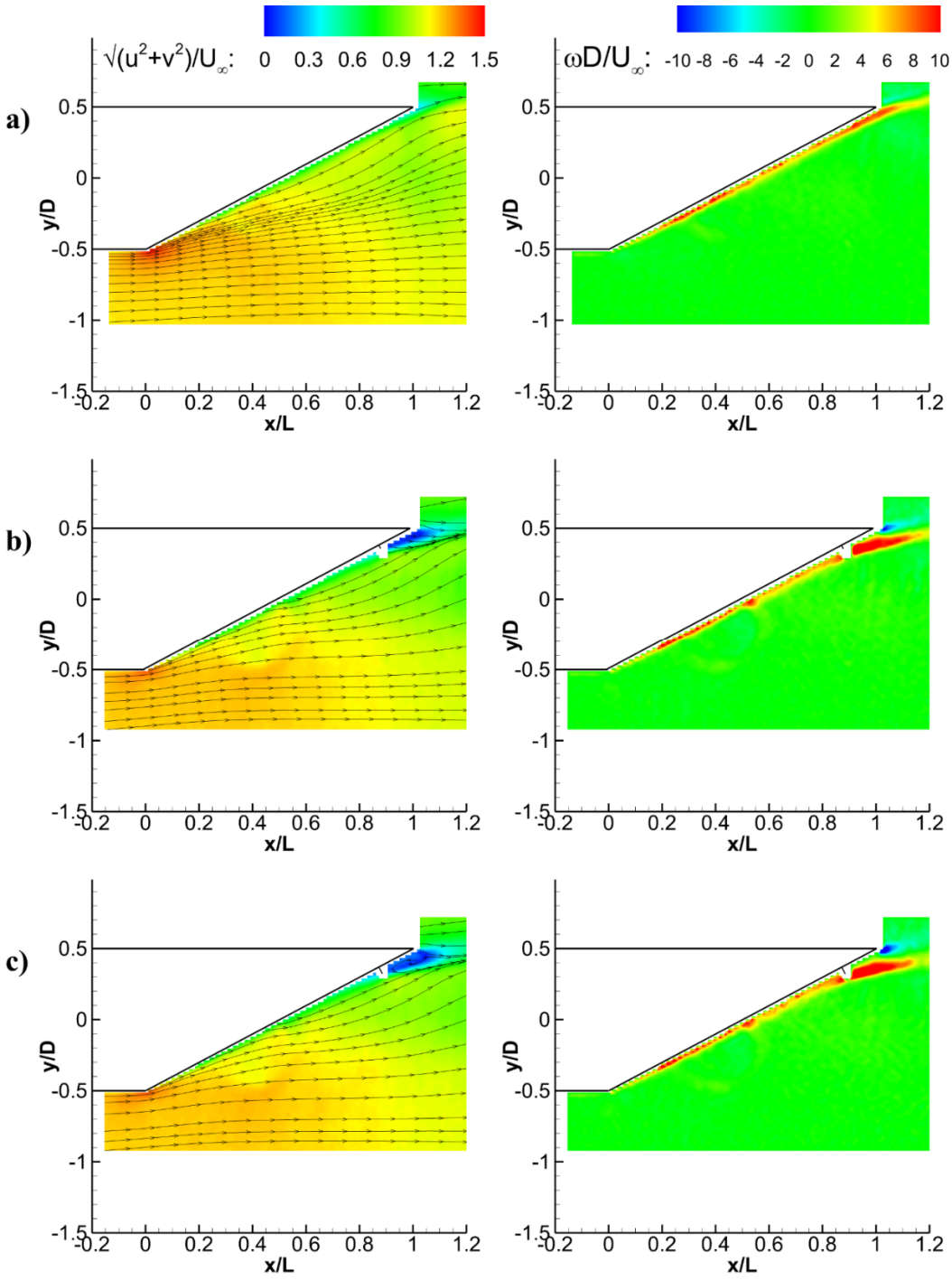

Figure 12: Time-averaged normalized velocity magnitude (left) and vorticity (right) on the *z*=0 plane for a) baseline case; and spoiler placed at x'_s/c = 87.5%, b) *h/D* = 2.5% and c) *h/D* = 5%.

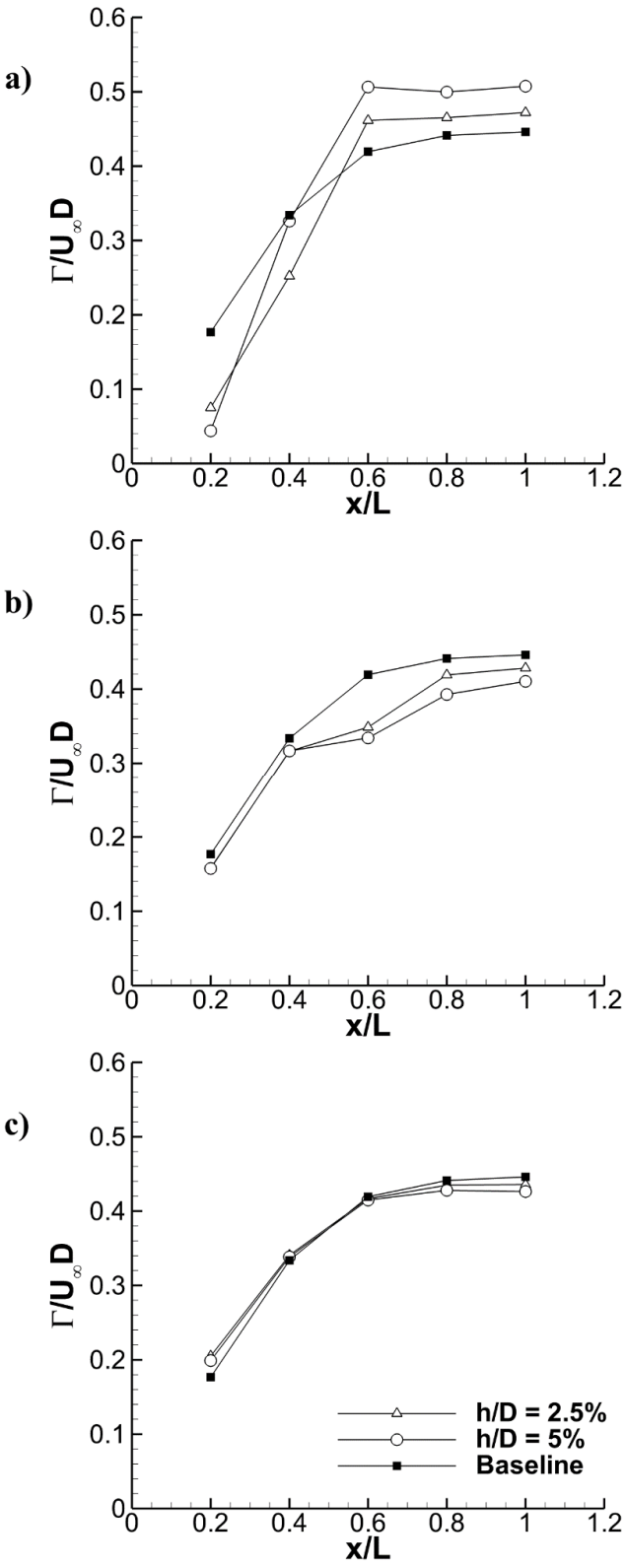

Figure 13: Variation of circulation for a) x'_s/c = 2.5%, b) x'_s/c = 47.5% and c) x'_s/c = 87.5%.

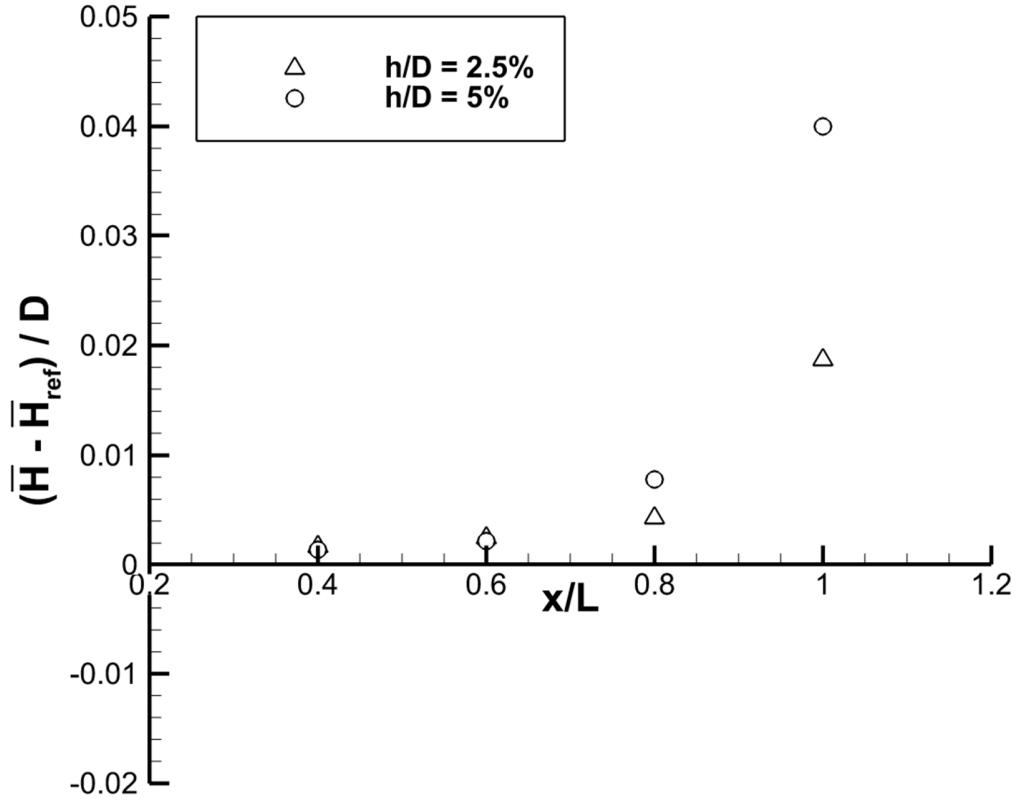

Figure 14. Vortex centroid locations for spoiler placed at x'_s/c = 87.5%.

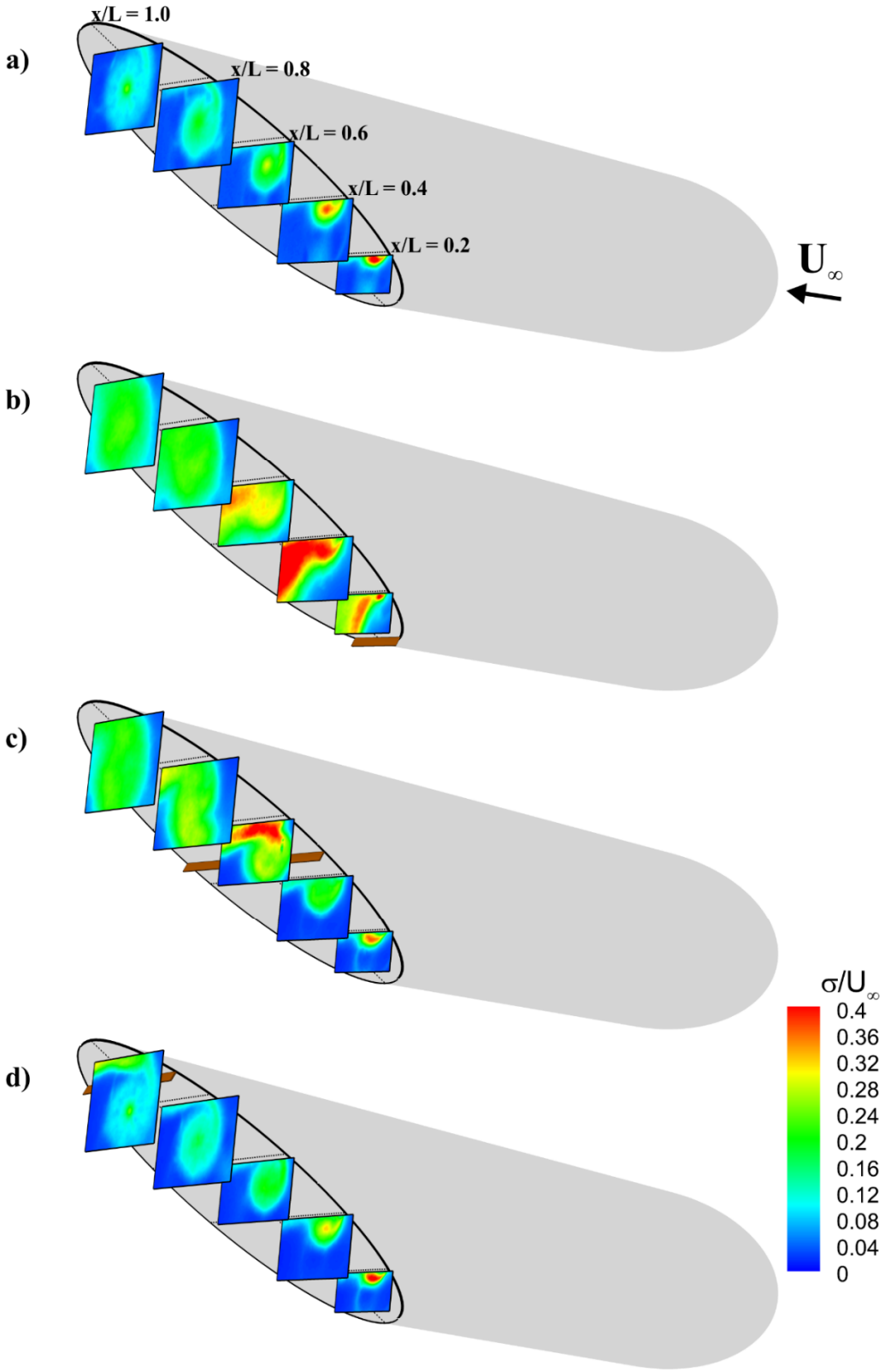

Figure 15: Three-dimensional perspective view of standard deviation of velocity for a) baseline case, b) x'_s/c = 2.5%, c) x'_s/c = 47.5% and d) x'_s/c = 87.5%. h/D = 5% for all cases.

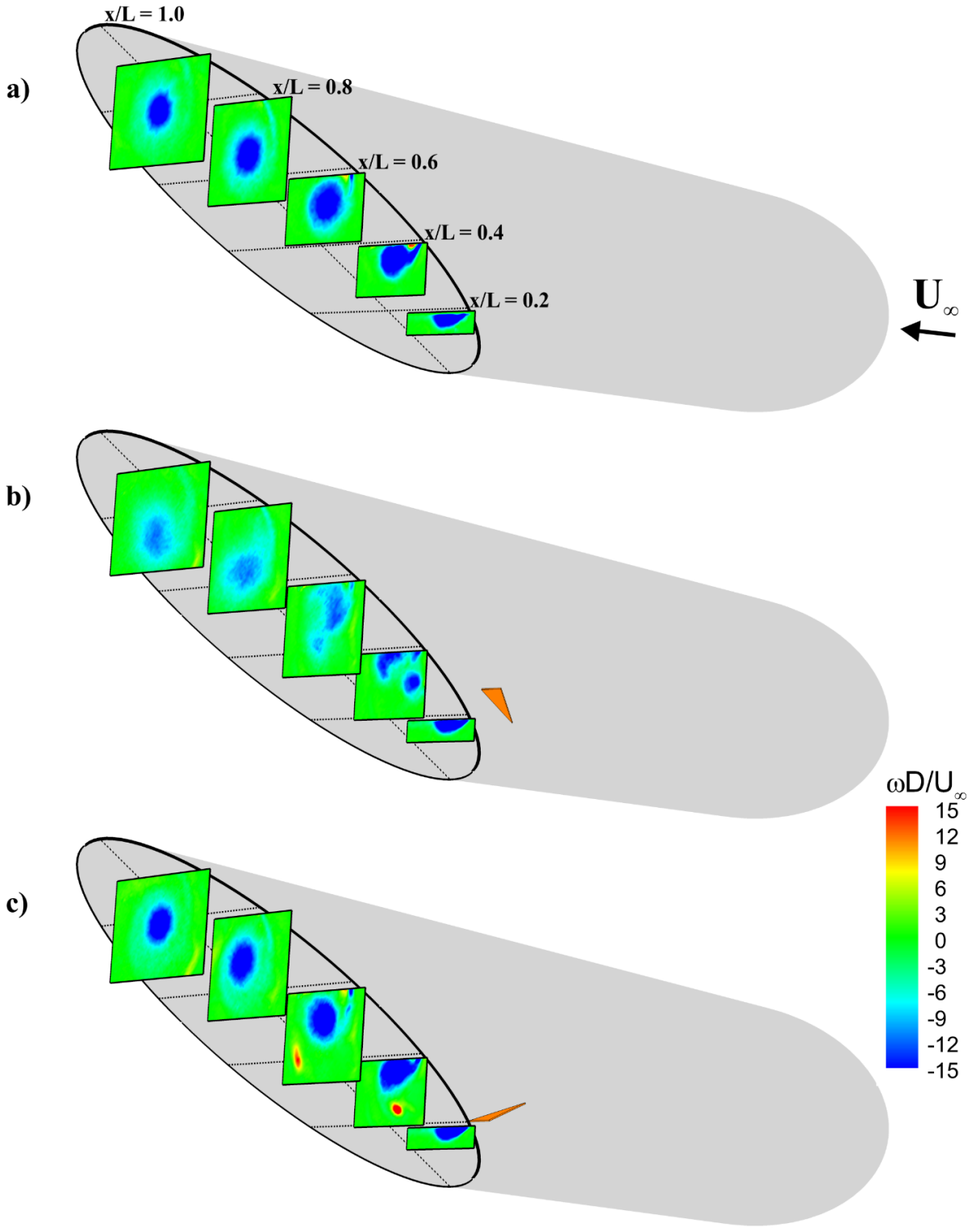

Figure 16: Three-dimensional perspective view of time-averaged vorticity for a) baseline case, b) co-rotating and c) counter-rotating cases. $\Lambda = 70°$, $\beta = 20°$.

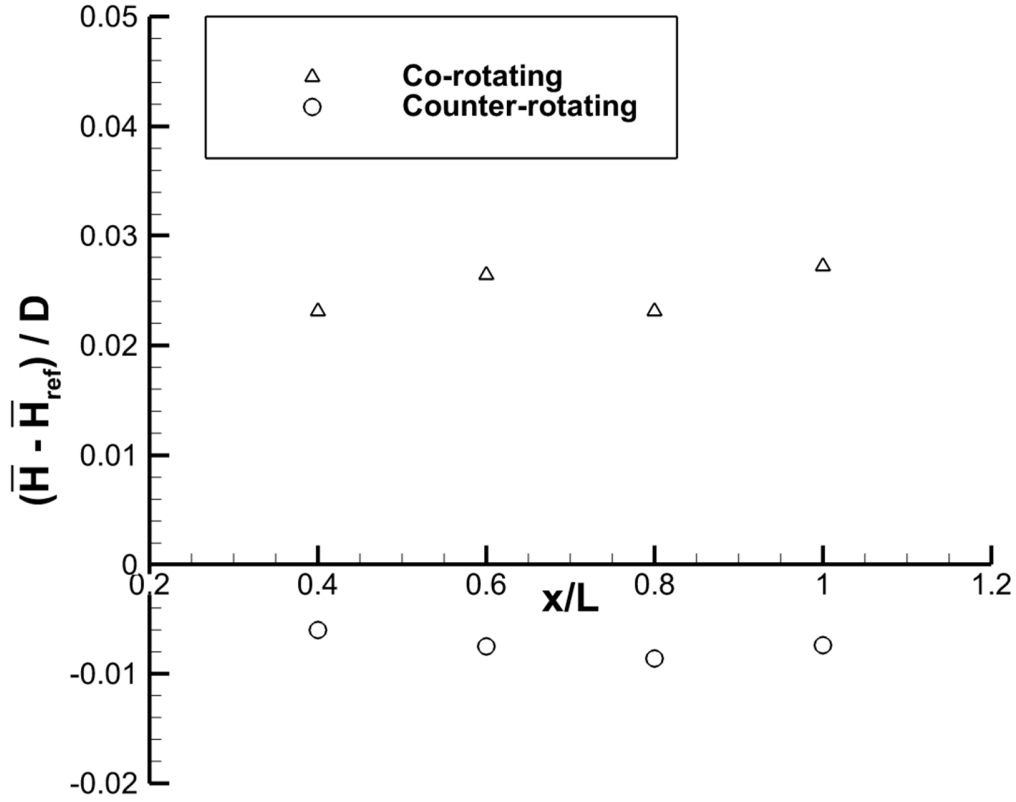

Figure 17. Vortex centroid locations for vortex generator configurations.